Ultralight and Highly Elastic Graphene/Lignin-Derived Carbon Nanocomposite Aerogels with Ultrahigh Electromagnetic Interference Shielding Performance

Zhihui Zeng,[a] Changxian Wang,[b,c] Youfang Zhang,[a] Peiyu Wang,[c] Seyed Ismail Seyed Shahabadi,[a] Yongmao Pei,[c] Mingji Chen,[*b] and Xuehong Lu[*a]

[a]School of Materials Science and Engineering, Nanyang Technological University, 50 Nanyang Avenue, Singapore 639798, Singapore

[b]Beijing Key Laboratory of Lightweight Multi-functional Composite Materials and Structures, Beijing Institute of Technology, Beijing 100081, China

[c]State Key Laboratory for Turbulence and Complex Systems, College of Engineering, Peking University, Beijing 100871, China

[*]E-mail: asxhlu@ntu.edu.sg (X. Lu); mjchen81@bit.edu.cn (M.C.).

Keywords: Lightweight, porous architectures, graphene, EMI shielding, high elasticity

Abstract: Ultralight and highly elastic reduced graphene oxide (RGO)/lignin-derived carbon (LDC) composite aerogels with aligned micron-sized pores and cell walls are prepared using a facile freeze-drying method. The presence of a small fraction of LDC in the cell walls enhances the interfacial polarization effect while almost maintaining the amount of charge carriers and conductivity of the cell walls, greatly boosting wave absorption capability of the cell walls. RGO/LDC aerogels also show a greater number of large cell walls with better integrity than RGO aerogels, further improving the multiple reflection ability of the aligned cell walls. Synergistic effects of the multi-phase cell walls and the preferred microstructures of the RGO/LDC aerogels lead to their high electromagnetic interference (EMI) shielding effectiveness of 21.3 to 49.2 dB at the ultralow density of 2.0 to 8.0 mg/cm^3. This corresponds to surface specific SE (SE divided by density and thickness) up to 53250 dB·cm^2/g, which is higher than reported values for other carbon- and metal-based shields. Furthermore, the critical roles that microstructures play in determining EMI shielding performance are directly revealed through comparing shielding performance in directions parallel and normal to cell walls, as well as in an in-situ compression process.

Introduction

Lightweight and compressible carbon-based porous architectures, which exhibit microcellular structures built with carbon nanomaterials, are currently attracting more and more attention as high-performance structural and functional materials.[1-10] These three-dimensional (3D) macroscopic structures are promising for many applications such as mechanical cushioning,[10] energy absorption,[9] and sensing.[8, 11] EMI shielding is also recently emerging as an important application for such 3D porous architectures.[12-16] Different from solid films whose EMI shielding performance is mainly dependent on bulk material properties, the shielding effectiveness (SE) of 3D porous architectures are influenced by both the properties of their intrinsic constituents and microstructures.[14, 17-19] The micron-sized pores in the porous architectures not only lead to weight reduction of the shields, but also embark multiple reflection effect[16, 20-22], resulting in extended path lengths of the incident waves in the porous architectures and hence increased absorption of electromagnetic waves by the constituents.

Since conventional metal-based shields typically suffer from high density and poor corrosion resistance, carbon nanomaterials such as carbon nanotubes (CNTs) and graphene have been intensively exploited for applications that require light-weight EMI shielding materials.[16, 23-31] In particular, graphene has a unique two-dimensional (2D) sp^2 network structure, exceptionally high carrier mobility, low density, extremely large specific surface area, superb mechanical strength and outstanding anti-corrosion property.[15,28-30,,32] It is, therefore, considered as an ideal building block for

constructing lightweight, robust and high-performance EMI shielding porous architectures, which are important for many application occasions such as aircraft, spacecraft, and portable electronics.[15,16,18,33] Specific SE (SSE), which is defined as the EMI SE divided by density of the shielding material, can be used to compare EMI shielding performance of materials with different densities.[13, 14, 34] Compared with the SSE of 10 dB·cm^3/g for copper-based shields at 3.1 mm thickness,[35] SSE values of around 64 and 40 dB·cm^3/g have been achieved for graphene embeded polystyrene [17] and polyetherimide [18] porous nanocomposites at 2.3-2.5 mm thickness, respectively. Graphene foams prepared by hydrazine foaming also showed higher SSE of 420 dB·cm^3/g and SE of 25.2 dB at thickness of 0.3 mm.[33] The good mechanical strength, high EMI SE and SSE of these graphene foams and polymer/graphene porous architectures can be attributed to the synergistic effects of their micron-sized pores and graphene constituents.

EMI shielding performance of a material mainly depends upon its reflection, absorption, and multiple reflection capability, which are associated with mobile charge carriers, electric dipoles, and large interfaces/surfaces in the shielding architectures, respectively.[32, 36-38] Total SE (SE_T) is the sum of shielding by reflection (SE_R) and absorption (SE_A), while multiple reflections can further enhance the absorption component owing to the extended path lengths of the waves in the shielding material. Generally, graphene-based porous macrostructures are constructed via either dispersing graphene layers into polymer matrices or directly assembling graphene-based foams. In the case of the former, interfaces are introduced between

the conductive graphene and insulating polymer matrices, and hence the interaction between electromagnetic fields and interfacial dipoles can cause a significant interfacial polarization loss, enhancing the SE_A.[21, 32, 36, 38, 39] However, the difficulty in achieving nanoscale dispersion of graphene layers in polymers and relatively high fractions of insulating polymers could result in a significant reduction of charge carriers and poor conductivity of the porous nanocomposites, which are detrimental to SE_A and SE_R, respectively.[13, 14, 17, 18, 20, 32] In the case of graphene-based foams, the presence of abundant charge carriers and excellent conductivity benefits the electric loss[37, 38] to the electromagnetic waves, improving the EMI shielding performance. However, it is desired to further improve the shielding performance of these foams by both enhancing the penetration loss of incident waves in the cell walls and extending path lengths of the incident waves in the foams via simultaneously manipulating the phase structure of the cell walls and microstructures of the foams. For example, CNT/ multilayered graphene hybrid foams fabricated by chemical vapor deposition (CVD) method,[15] graphene embedded in the carbon-based foams prepared by phase separation and graphitization,[25] multiwall carbon nanotube (MWCNT)/graphene foams obtained by solvothermal method[40] were designed to improve penetration loss ability of the cell walls. These composite or hybrid foams showed enhanced EMI shielding performance or microwave absorption ability, such as ultrahigh SSE values up to around 10000 $dB \cdot cm^3/g$. The pore structures of these foams were, however, not tailored to further enhance their EMI shielding performance via boosting the multiple reflection effect. Since the constituents and phase structure of the cell walls, the

morphology of the cell walls, and pore structure of the foams are all vitally important factors for enhancing EMI shielding performance, a new strategy needs to be designed to simultaneously manipulate these factors to realize mechanically robust graphene-based porous architectures that are efficient in multiple reflections[39-44], and exhibit significant polarization loss while retaining abundant charge carriers and high conductivity.

In this work, to address the above issue, we designed and fabricated a novel 3D unidirectional porous architecture with cell walls composed of reduced graphene oxide (RGO) layers and lignin-derived carbon (LDC). Lignin, a type of natural macromolecules obtained as a byproduct in paper manufacturing industry,[45] has been used to construct various types of LDC-based porous architectures.[47,48] In our design, the presence of LDC in the RGO-based cell walls results in the formation of interfaces between the RGO layers and LCD and thus improves the interfacial polarization effect of the nanocomposites,[32, 38] while abundant charge carriers and high electrical conductivity of the graphene layers can be well retained with a low content of LDC; the LCD phase also provides additional intrinsic charge carriers. Furthermore, with lignin as "glue" between GO layers, extremely high and controlled porosity, and well aligned micron-sized pores can be created using a facile ice-templating method,[7, 49-51] resulting in thin yet tight unidirectional RGO/LDC cell walls after the carbonization, and hence leading to improved multiple reflection capability. Owing to these unique multi-phase and microstructural characteristics, the RGO/LDC foams can reach an EMI SE of 21.3 to 49.2 dB at a thickness of 2.0 mm and ultralow density of 2.0 to 8.0

mg/cm^3, corresponding to the extremely high SSE of 10650 dB·cm^3/g and surface SSE (SSE divided by the thickness) of 53250 dB·cm^2/g, which are higher than those reported for other carbon- and even metal-based shields. In addition, the incorporation of LDC and the honeycomb-like microstructure lead to significantly enhanced mechanical strength and relatively high elasticity of the RGO/LDC aerogels. EMI shielding performance of the aligned porous architectures is also measured in an in-situ compression process, and the variation of the EMI shielding behavior with compression demonstrates, directly, the critical influences of the microstructures on the EMI shielding performance.

Experimental Section

***Fabrication of graphene based aligned porous architectures*:** Through a modified Hummer's method, GO dispersed in water suspension was prepared with controlled concentration. [54] The alkali lignin (USA, TCI product number: L0082, soft lignin) water suspension with the same concentration as the GO suspension was adjusted and mixed with various ratios by the magnetic stirring for 3 h. By freezing the mixed aqueous suspensions in a mold with Teflon jacket and stainless steel bottom using liquid nitrogen, the ice-crystal nuclei formed rapidly at the bottom of the mixed suspensions, and the large temperature gradient could result in unidirectional growth of the ice crystals towards the top of the mold. Simultaneously, the dispersed GO/lignin in the suspension were excluded to stay between the ice crystals to form the

GO/lignin composite cell walls. Subsequently, through freeze-drying in a freeze-drying vessel (–80 ^{o}C and 10 Pa) for 24 h to sublimate the ice, porous GO/lignin foams with aligned GO/lignin composite cell walls were formed. Finally, the foams were heated at a rate of 5 ºC/min in a tube furnace and carbonized at the temperature of 900 ºC for 2 h under argon atmosphere to obtain the aligned porous RGO/LDC aerogels. Density of the GO/lignin foams and relevant RGO/LDC aerogels could be controlled by adjusting the water fraction of the mixed aqueous suspension. Lower water fraction could result in higher densities of the GO/lignin foams and RGO/LDC aerogels. The content of the RGO/LDC in the aerogels could also be controlled by tuning the ratio of the lignin to GO in the aqueous solution. For example, by mixing 7.5 mg/ml RGO and 7.5 mg/ml lignin suspensions at equal amount and treating the mixture following the procedure described above, the GO/lignin foams with 50 wt% lignin and density of around 12 mg/cm^3 were prepared, and the corresponding RGO/LDC composite aerogels were obtained by further carbonization. Also, various shapes or sizes of the aerogels were obtained by selecting various molds. After the same freeze-drying process and carbonization treatment of the GO or lignin suspension, RGO or LDC aerogels were obtained as well.

***Characterization*:** Microstructure of the porous architectures was investigated by scanning electron microscopy (SEM, JSM-7600F). The resistance (R) of the sample was measured by four-probe method with a Keithley 4200-SCS Semiconductor Characterization System (Keithley, Cleveland, Ohio, USA) at room temperature. The electrical conductivity (σ) was obtained by the equation $\sigma = 1 / (R \cdot A)$, where A and l

are the effective area and length of the measuring electrode, respectively. The compression behavior of the porous sample was evaluated using a dynamic mechanical analyzer (DMA, TA Q800), and the loading applied was cyclic in DMA strain rate mode. The dimensions of the tested samples were 1 × 1 × 1 cm^3, and at least five specimens for each type of aerogels were tested. The carbon-based aerogels were compressed in the transverse direction, i.e., the direction normal to the aligned cell walls, and longitudinal direction, i.e., the direction parallel to the orientation direction of the cell walls, respectively, and thus transverse and longitudinal mechanical stress-strain curves were obtained, respectively. EMI SE characterizations were carried out on the samples with size of 22.86 mm × 10.16 mm (length × width) in the frequency range of 8.2–12.4 GHz (X-band), by a waveguide method using a vector network analyzer (Agilent E8363B PNA-L), and more than five specimens were tested for each type of foams. The *S*-parameters of each sample were recorded and applied to calculate the EMI SE. It is worth noting that the sample thickness could be adjusted but it could not be larger than 9.46 mm because the waveguide chamber's dimensions were 22.86 mm (length) × 10.16 mm (width) × 9.46 mm (thickness). The electric filed direction was in the width direction and the propagation direction of tested wave was in the thickness direction of the waveguide chamber. In the case of longitudinal EMI SE measurement, EMI SE values were measured when the incident wave propagated parallel to the cell walls' direction (Z direction shown in Figure 1a). In the case of transverse EMI SE measurement, the propagation direction of incident

wave was normal to the cell walls' direction (normal to Z direction), and the electric direction was parallel to the cell walls' direction (Z direction).

Results and Discussion

To prepare the RGO/LDC aerogels, GO with average lateral size of 10 μm was synthesized and uniformly dispersed in water (Figure S1a), followed by mixing with a lignin suspension (**Figure 1**a-i). Zeta potentials of the GO and mixed suspension with GO/lignin mass ratio of 1:1 are lower than -30 mV, showing moderate stability of the suspensions and indicating their feasibility for freeze-drying process (Figure S1b). In the freezing process, the steep temperature gradient results in the rapid formation of ice-crystal nuclei at the bottom of the mixed suspensions and unidirectional growth of ice crystals towards top, and the dispersed GO sheets and lignin molecules are excluded to form cell walls between ice crystals (Figure 1a-ii). After the freeze-drying process, the ice crystals are sublimated and thus the GO/lignin foams with aligned micron-sized pores and cell walls are obtained (Figure 1a-iii, Figure 1b-e). Herein the parallel and perpendicular directions to the growth direction of ice crystals in the suspension are defined as the longitudinal (Z direction) and transverse directions (X or Y direction), respectively, and hence the resultant porous architectures have aligned cell walls in longitudinal direction. In a subsequent carbonization treatment (Figure 1a-iv), majority of oxygen-containing groups in GO is removed and the lignin is carbonized (Figure S2, Figure S3, Table S1), resulting in the formation of RGO/LDC aligned porous aerogels (Figure 1f-i). Compared with GO/lignin

nanocomposites with smooth cell walls, RGO/LDC aerogels have wrinkled cell walls (Figure 1e, i). In addition to tuning macroscopic shape and size (Figure 1b, f), porosity and density of the foams can be controlled easily by adjusting water fraction in the suspension before freezing. The outstanding mechanical property of interconnected cell walls and the adjustable high porosity lead to the production of stable, large-dimension, free-standing RGO/LDC aerogels with ultralow density down to 2.5 mg/cm^3 (Figure 1f-i, Figure S4).

Synergistic actions of the graphene layers and LDC lead to the improvements in macroscopic performance and microscale structures. Owing to the vast weight loss of the lignin in the carbonization process (Figure S5a), the LDC aerogels have severe volume contractions (**Figure 2**a, Figure S5b). However, outstanding mechanical modulus of the graphene layers can result in enough strength of cell walls to sustain the RGO/LDC or RGO aerogels, and provide dimensional stability. Nonetheless, after carbonization, pure LDC aerogels show much higher density, resulted from large volume shrinkage. GO/lignin nanocomposites, on the other hand, produce RGO/LDC aerogels with relatively lower densities (Figure 2b). The lower conductivity and C/O ratio of the carbon, compared with those of the RGO, also result in slightly lower conductivity for the RGO/LDC aerogels made from GO/lignin composites with higher lignin contents (Figure 2b,c, Table S1). After the same carbonization treatment of GO, lignin and GO/lignin foams with the similar densities (~ 12 mg/cm^3) (Figure S6), RGO, LDC and RGO/LDC aerogels, with evident aligned cell walls, are obtained, respectively (Figure 2d-f, Figure S7). Owing to the molecular nature of lignin, it gives

stronger interactions between the constituents than GO, leading to thicker cell walls and better integrity for the lignin foams, while thinner and holey cell walls are observed for the GO foams (Figure S6a-b). In GO/lignin foams, the composite of the lignin and GO leads to relatively thin cell walls, while the integrity of the cell walls is maintained simultaneously (Figure S6c). Therefore, RGO/LDC aerogels own more intact cell walls with better integrity than RGO aerogels (Figures S7a, c, d, e), and thinner cell walls (tens of nanometers) than LDC aerogels (around hundreds of nanometers) (Figure S7b). If the lignin content is too high, the RGO/LDC aerogels will shrink significantly, and hence have thicker cell walls and smaller spacing between the cell walls than those of neat RGO aerogels. Nevertheless, abundant composite cell walls with good integrity can be obtained by adjusting the initial lignin content, which would result in large effective cell-wall surface area for multiple reflection (Figure 2f, Figure S7c, e), and hence potentially improve the multiple reflection capability of the RGO/LDC aerogels.

Microstructures of the foams also play critical roles in determining their compressive modulus and elastic performance. For all the foams studied in this work, longitudinal modulus obtained by compressing the sample in the longitudinal direction is much higher than the transverse one, attributed to more sustained cell walls in the longitudinal direction (Figure 2g, Figure S8). However, RGO/LDC aerogels show complete recovery and excellent reversibility after the application of various compressive strains even up to 70 % in the transverse direction (Figure 2g), while they cannot recover fully under the compressive strain of 50 % in the

longitudinal direction (Figure S8). Even after 300 compression cycles in the transverse direction, compressive stress of the RGO/LDC aerogels at a high strain of 50 % is only decreased by less than 10 %, which displays their high elasticity and good cycling stability (Figure 2h,i).[2] Similar compressive behavior is observed for RGO and LDC aerogels; however, the mechanical strength and modulus of RGO/LDC aerogels are improved over their RGO counterparts due to the presence of a small amount of LDC in RGO aerogels (Figure S9). The LDC aerogels have higher compressive modulus because of their significantly higher density. However, compared with RGO and RGO/LDC aerogels, LDC aerogels display higher stress reduction ratio under the cyclic compressive curve probably because LDC-based cell walls with lower modulus have poorer elastic performance[2] (Figure 2i). In short, the RGO/LDC aerogels exhibit considerable mechanical strength and good elasticity due to their microstructural character, which is of vital importance for achieving robust EMI shielding materials for practical applications.

EMI SE is measured first when incident wave propagation is parallel to the transverse direction of the aligned porous aerogels. SE is almost independent of the frequency, implying the uniform microstructure and conductivity of the porous architectures (**Figure 3**a).[52] Initially, EMI SE of the RGO/LDC aerogels increases with increasing LDC content, whereas after reaching a maximum it starts to decrease at higher LDC contents. LDC and RGO aerogels show SE of 6.1 dB and 22.3 dB, respectively, at the thickness of 2 mm. RGO/LDC aerogels made from the GO/lignin foams with small fraction of lignin ranging from 9.1 wt% to 25 wt%, on the other

hand, all show higher EMI SE (30.9 to 26.9 dB) than both LDC and RGO aerogels at the same thickness. Although slight decrease in SE_R of RGO/LDC aerogels is observed with increased LDC content, which is because of decreased conductivity, the SE_A show more notable increase and hence the EMI SE increases (Figure 3b). The RGO/LDC aerogels made from GO/lignin foams with 9.1 wt% to 25 wt% lignin exhibit SE_A ranging from 26.4 dB to 22.2 dB. By contrast, the RGO foams show SE_A of only 17.7 dB. Higher lignin content, e.g., 50.0 wt%, in GO/lignin composites may be more detrimental to conductivity and also reduce charge carriers in the corresponding RGO/LDC aerogels significantly, resulting in a decrease in total EMI SE (14.3 dB).

The data presented above indicate that the introduction of LDC into the cell walls of the RGO-based aerogels has played critical roles in improving the EMI shielding performance of the aerogels. Firstly, the addition of a small fraction of LDC to RGO/LDC aerogels does not noticeably reduce the amount of charge carriers or deteriorate bulk conductivity. Secondly, the LDC can introduce substantial interfacial area between the carbon and graphene layers in the cell walls. According to Maxwell-Wagner-Sillars polarization principle,[32] the conductivity mismatch between the LDC and RGO in the composite cell walls can result in polarization and charge accumulation at their interfaces in the electromagnetic field, which can further interact with the incident electromagnetic waves. Therefore, high electric loss of the composite cell walls to the incident electromagnetic waves derived from the maintained conductivity and charge-carrier amount, and the effective interfacial

polarization[22, 23] resulted from the interfaces between LDC and RGO can both improve intrinsic absorption ability of the RGO/LDC composite cell walls. Moreover, the presence of LDC also leads to larger effective cell-wall surface area for reflection, causing enhanced multi-reflection of the incident waves. Thus, even with a small fraction of LDC, the coexistence of these characteristics can lead to significantly higher SE_A and SE_T of the RGO/LDC composite aerogels than those of RGO. For example, EMI SE values of neat RGO aerogels are only 22.3 and 14.2 dB at the densities of 4.5 and 3.0 mg/cm^3, respectively, while the RGO/LDC aerogel with a small fraction of LDC, which was made from GO/lignin with 25 wt% lignin, exhibits EMI SE of 30.0 and 21.3 dB at the densities of 4.5 and 2.0 mg/cm^3, respectively (Figure 3c); the thickness is 2 mm for both types of aerogels.

To further verify contribution of the LDC to the EMI shielding performance, theoretical EMI SE values (M-SE_T, M-SE_R, M-SE_A) calculated based on the conductivity of a homogeneous shield (the calculation method is shown in Supporting Information) are compared with the measured SE values (SE_T, SE_R, SE_A) in Figure 3b. Without LDC, the calculated M-SE_T is higher than the experimentally measured SE_T of the RGO aerogel, which may be attributed to the detrimental effect of the very high porosity (Table S1) on the shielding performance. By contrast, in the case of RGO/LDC composite aerogels with optimized cell walls, the experimentally measured SE_A values are much higher than the corresponding M-SE_A values because the latter are calculated without considering the multi-phase structure of the RGO/LDC cell walls and their large effective surface area for multiple reflection.

Since the differences between M-SE_R and SE_R of these composite aerogels are very small at similar conductivities, the experimentally measured SE_T values are also much higher than the corresponding M-SE_T values.

In addition to the LCD content, the density and thickness of the RGO/LDC composite aerogels can also be controlled easily to adjust their EMI SE values. Since higher density or larger thickness of the composite aerogels can lead to more charge carriers and interfacial dipoles interacting with the incident electromagnetic waves, EMI SE of the aerogels typically increases with the density and thickness. For example, EMI SE of this composite aerogel made from GO/lignin with 25 wt% lignin can reach as high as 49.2 dB at a density of 8.0 mg/cm^3. The ultralight RGO/LDC aerogel with density 2.5 mg/cm^3 also shows an EMI SE as high as around 80 dB at the thickness of 9 mm (Figure 3d). It is also worth noting that at the thickness of only 2 mm and ultralow density of 2.5 mg/cm^3, EMI SE of the RGO/LDC aerogel is well above 20 dB, which is high enough for commercial EMI shielding applications. Considering the influences of the density and thickness on the EMI shielding performance, in order to make a clearer comparison, SSE/*d* (SE normalized by thickness and density) of typical shielding materials as a function of density are presented in Figure 3e, and a comprehensive comparison with more reported data is given in Table S2. The excellent EMI SE of the graphene-based porous architectures reported in this work, which are achieved at an ultralow density and low thickness, results in exceptionally high values for SSE and SSE/*d* (Table S2). The SSE values of the RGO/LDC aerogels can reach as high as 32000 dB·cm^3/g, which are much higher

than those of other previously reported shielding materials at the similar thicknesses. For example, some reported superb SSE values include 500 dB·cm^3/g for graphene/PDMS composite foams,[16] 1148 dB·cm^3/g for CNT/WPU foams,[14] 1100 dB·cm^3/g for a CNT sponge,[43] 3122 dB·cm^3/g for graphene/PEDOT:PSS composite foams,[53] and 6600-11300 dB·cm^3/g for CNT/graphene foams,[15] which are all lower than the aforementioned SSE values of our RGO/LCD aerogels (Table S2). The SSE/*d* values of the RGO/LDC aerogels range from 30750 to 57200 dB·cm^2/g, which far exceed those of most shielding materials. For example, even satisfying the commercial EMI SE level, SSE/*d* of the RGO/LDC aerogels with 2-mm thickness can reach as high as 53250 dB·cm^2/g, which is comparable to recently reported extremely high values of 40000 dB·cm^2/g for the CNT/multilayer graphene foams[15] and 30830 dB·cm^2/g for the $Ti_3C_2T_x$ film[34], as well as 30555 dB·cm^2/g for a pure metal (Al foil) [34]. Furthermore, the controllability of the density and thickness for these aerogels is also an important feature which allows us to easily obtain adjustable and controllable SE and SSE. This feature, along with good mechanical performance of these aerogels, brings about great potentials for these graphene-based aligned porous aerogels for practical applications.

To thoroughly analyze the roles that micron-sized pores play in the EMI shielding performance of the porous architecture, the longitudinal EMI SE (L-SE_T, L-SE_A and L-SE_R), referring to SE when wave propagation is parallel to the longitudinal direction, is compared with the transverse SE (T-SE_T, T-SE_A and T-SE_R). The SE_T, SE_A, and SE_R of the RGO/LDC aerogels (made from GO/lignin foams with

25 wt% lignin) at 10 GHz and at the thickness of 6 mm are shown as functions of sample density in both directions (Figure 3f). We can observe that T-SE_A is much higher than L-SE_A, while T-SE_R and L-SE_R are similar. Therefore, for aerogels at the same thickness and density, T-SE_T is much higher than L-SE_T. In the case of the aligned porous aerogels, the incident waves passing along the transverse direction can interact with significantly more cell walls. As a result, considering the good absorption ability of the cell walls, T-SE_A becomes much larger than L-SE_A. SE_R, however, is related to conductivity which is similar in both directions, hence the corresponding values are similar. Therefore, T-SE_T becomes much higher than the L-SE_T, thanks in large to SE_A. For example, L-SE_A and T-SE_A can reach 33.5 dB and 67.2 dB, respectively, which can result in L-SE_T and T-SE_T values of 35.8 dB and 71.0 dB, respectively. Significant difference in the longitudinal and transverse absorptions, therefore, well demonstrate the important influence of micron-sized pores on the EMI shielding performance.

To further investigate the influences of the micron-sized pores on the EMI shielding performance, the EMI SE is obtained for RGO/LDC aerogels subjected to compression in transverse direction. With an increased compressive strain, more voids disappear from the aerogels and interconnections and contacts between the cell walls are increased (**Figure 4**a), resulting in increased density and electrical conductivity for the aligned porous architectures (Figure 4b). Compression-induced increase in the conductivity of aerogels leads to an enhanced SE_R. By contrast, owing to decreased cell-wall surfaces that are squeezed together with increased compression strain, the

compression reduces the pores and in turn the multiple reflections and, as a result, SE_A reduces. As absorption dominates total shielding, EMI SE_T decreases with increased compressive strain. In short, compressing aerogels, which changes microstructure and in turn the contributions from different EMI shielding mechanisms, provides another direct proof on the critical roles that micron-sized pores play in the EMI shielding performance. Moreover, EMI SE can still be maintained without noticeable deterioration even after 100 deformation cycles up to 50 % compressive strain (Figure 4c), demonstrating the durability of our robust RGO/LDC aerogels for EMI shielding applications. Based on the results presented above, we propose a mechanism to explain the exceptionally high EMI shielding performance of the ultralight weight RGO/LDC aerogels (Figure 4d). Owing to the unidirectionally aligned cell walls and their good integrity, the incident electromagnetic waves can meet and interact effectively with much larger area of cell-wall surfaces in the transverse direction, leading to a significantly enhanced multiple reflection ability of the aerogels. This, combined with the high absorption ability of the cell walls derived from interfacial polarization at RGO-LDC interfaces and abundant charge carriers-induced electric loss in the RGO/LDC composite cell walls, gives our RGO/LDC aerogels excellent EMI SE at ultralow density and thereby super high SSE and SSE/*d*.

Conclusions

Ultralight, highly elastic, and robust RGO/LDC aerogels, featuring aligned micron-sized pores and cell walls, are fabricated using a simple freeze-drying method. RGO/LDC aerogels show a greater number of large cell walls with good integrity than RGO aerogels, and thinner and more cell walls than LDC aerogels. A larger amount of tight cell walls results in larger effective cell-wall surface area for reflection, improving the multiple reflection ability of the aerogels. The enhanced multiple reflection effect, combined with high wave absorption ability derived from abundant charge carriers and interfacial polarization dipoles in the cell walls, result in exceptionally high EMI shielding performance of these lightweight aerogels. The density and size of our RGO/LDC aerogels also show good controllability for achieving a wide range of EMI SE. EMI SE of the 2 mm thick RGO/LDC composite aerogels can reach up to 49.2 and 21.3 dB at ultralow low densities of 8.0 and 2.0 mg/cm^3, respectively. At a density of 2.5 mg/cm^3, the RGO/LDC aerogels can also show high EMI SE of 80.0 to 23.2 dB by adjusting the thickness of the samples. The SSE/d value can achieve up to 53250 dB·cm^2/g that is higher than values reported for other of carbon- and even metal-based shields. Furthermore, by comparing shielding performance of the aerogels in transverse and longitudinal directions, as well as in a compression process, it is directly proved that the micron-sized pores play a critical role in determining the absorption ability of the RGO/LDC composite cell walls. These 3D macrostructures with optimized microstructures in terms of cell walls and micron-sized pores, combined with ultralow density, high electrical conductivity, considerable mechanical strength, and high elasticity, underscore the great potential of

these RGO/LDC aerogels as ultralight, robust, and ultrahigh performance EMI shielding materials for practical applications.

ASSOCIATED CONTENT

(S) Supporting Information

Optical images of as-prepared GO, FTIR, Raman, XPS, SEM, TGA and mechanical properties of as-prepared aerogels, theoretically calculated EMI shielding performance of a homogeneous shield, and the table for EMI shielding performance of various shielding materials are included in the **Supporting Information**, which is available free of charge on the **ACS Publications website** at **http://pubs.acs.org**.

AUTHOR INFORMATION

Corresponding Author

E-mail: asxhlu@ntu.edu.sg (Xuehong Lu); mjchen81@bit.edu.cn (Mingji Chen)

Conflicts of interest

There are no conflicts of interest to declare

ACKNOWLEDGMENTS

The authors thank Nanyang Technological University and Agency for Science, Technology, and Research, Singapore, for providing funding and Ph.D. scholarships throughout this work.

REFERENCES

(1) Chen, Z.; Ren, W.; Gao, L.; Liu, B.; Pei, S.; Cheng, H.-M. Three-dimensional Flexible and Conductive Interconnected Graphene Networks Grown by Chemical Vapour Deposition. *Nat. Mater.* **2011**, *10*, 424-428.

(2) Gao, H. L.; Zhu, Y. B.; Mao, L. B.; Wang, F. C.; Luo, X. S.; Liu, Y. Y.; Lu, Y.; Pan, Z.; Ge, J.; Shen, W.; Zheng, Y. R.; Xu, L.; Wang, L. J.; Xu, W. H.; Wu, H. A.; Yu, S. H. Super-elastic and Fatigue Resistant Carbon Material with Lamellar Multi-Arch Microstructure. *Nat. Commun.* **2016**, *7*, 12920.

(3) Ge, J.; Shi, L. A.; Wang, Y. C.; Zhao, H. Y.; Yao, H. B.; Zhu, Y. B.; Zhang, Y.; Zhu, H. W.; Wu, H. A.; Yu, S. H. Joule-heated Graphene-wrapped Sponge Enables Fast Clean-up of Viscous Crude-oil Spill. *Nat. Nanotechnol.* **2017**, *12*, 434-440.

(4) Hu, H.; Zhao, Z.; Wan, W.; Gogotsi, Y.; Qiu, J. Ultralight and Highly Compressible Graphene Aerogels. *Adv. Mater.* **2013**, *25*, 2219-2223.

(5) Luo, S.; Luo, Y.; Wu, H.; Li, M.; Yan, L.; Jiang, K.; Liu, L.; Li, Q.; Fan, S.; Wang, J. Self-assembly of 3D Carbon Nanotube Sponges: A Simple and Controllable Way to Build Macroscopic and Ultralight Porous Architectures. *Adv. Mater.* **2017**, *29,* 1603549.

(6) Zhu, C.; Han, T. Y.; Duoss, E. B.; Golobic, A. M.; Kuntz, J. D.; Spadaccini, C. M.; Worsley, M. A. Highly Compressible 3D Periodic Graphene Aerogel Microlattices. *Nat. Commun.* **2015**, *6*, 6962.

(7) Qiu, L. ; Liu, J. Z. ; Chang, S. L. ; Wu, Y.; Li, D. Biomimetic Superelastic Graphene-based Cellular Monoliths. *Nat. Commun.* **2012**, *3*, 1241.

(8) Qiu, L.; Bulut Coskun, M.; Tang, Y.; Liu, J. Z.; Alan, T.; Ding, J.; Truong, V. T. Li, D. Ultrafast Dynamic Piezoresistive Response of Graphene-Based Cellular Elastomers. *Adv. Mater.* **2016**, *28*, 194–200.

(9) Zhang, Y.; Huang, Y. ; Zhang, T.; Chang, H. ; Xiao, P.; Chen, H. ; Huang, Z.; Chen, Y. Broadband and Tunable High-performance Microwave Absorption of An Ultralight and Highly Compressible Graphene Foam. *Adv. Mater.* **2016**, *27*, 2049-2053.

(10) Kim, K. H. ; Oh, Y. ; Islam, M. F. Graphene coating makes carbon nanotube aerogels superelastic and resistant to fatigue. *Nat. Nanotechnol.* **2012**, *7*, 562-566.

(11) Qin, Y.; Peng, Q.; Ding, Y.; Lin, Z. ; Wang, C.; Li, Y.; Xu, F.; Li, J.; Yuan, Y.; He, X.; Li, Y. Lightweight, Superelastic, and Mechanically Flexible Graphene/Polyimide Nanocomposite Foam for Strain Sensor Application. *ACS Nano* **2015**, *9*, 8933-8941.

(12) Yang, Y.; Gupta, M. C.; Dudley, K. L.; Lawrence, R. W. Novel Carbon Nanotube−Polystyrene Foam Composites for Electromagnetic Interference Shielding. Nano Lett. 2005, 5, 2131-2134.

(13) Yang, Y.; Gupta, M. C.; Dudley, K. L.; Lawrence, R. W. Conductive Carbon Nanofiber–Polymer Foam Structures. Adv. Mater. 2005, 17, 1999-2003.

(14) Zeng, Z.; Jin, H.; Chen, M.; Li, W.; Zhou, L.; Zhang, Z. Lightweight and Anisotropic Porous MWCNT/WPU Composites for Ultrahigh Performance Electromagnetic Interference Shielding. Adv. Funct. Mater. 2016, 26, 303-310.

(15) Song, Q.; Ye, F.; Yin, X.; Li, W.; Li, H.; Liu, Y.; Li, K.; Xie, K.; Li, X.; Fu, Q.; Cheng, L.; Zhang, L.; Wei, B. Carbon Nanotube-Multilayered Graphene Edge Plane Core-Shell Hybrid Foams for Ultrahigh-Performance Electromagnetic-Interference Shielding. *Adv. Mater.* **2017**,1701583.

(16) Chen, Z.; Xu, C.; Ma, C.; Ren, W.; Cheng, H. M. Lightweight and Flexible Graphene Foam Composites for High-performance Electromagnetic Interference Shielding. *Adv. Mater.* **2013,** *25*, 1296-1300.

(17) Yan, D.-X.; Ren, P.-G.; Pang, H.; Fu, Q.; Yang, M.-B.; Li, Z.-M. Efficient Electromagnetic Interference Shielding of Lightweight Graphene/Polystyrene Composite. *J. Mater. Chem.* **2012,** *22*, 18772-18774.

(18) Ling, J.; Zhai, W.; Feng, W.; Shen, B.; Zhang, J.; Zheng, W. Facile Preparation of Lightweight Microcellular Polyetherimide/Graphene Composite Foams for Electromagnetic Interference Shielding. *ACS Appl. Mater. Interfaces* **2013,** *5*, 2677-2684.

(19) Ameli, A.; Nofar, M.; Wang, S.; Park, C. B. Lightweight Polypropylene/Stainless-Steel Fiber Composite Foams with Low Percolation for

Efficient Electromagnetic Interference Shielding. *ACS Appl. Mater. Interfaces* **2014,** *6*, 11091-11100.

(20) Shen, B.; Zhai, W.; Tao, M.; Ling, J.; Zheng, W. Lightweight, Multifunctional Polyetherimide/Graphene@Fe3O4 Composite Foams for Shielding of Electromagnetic Pollution. *ACS Appl. Mater. Interfaces* **2013,** *5*, 11383-11391.

(21) Ameli, A.; Jung, P. U.; Park, C. B. Electrical Properties and Electromagnetic Interference Shielding Effectiveness of Polypropylene/Carbon Fiber Composite Foams. *Carbon* **2013,** *60*, 379-391.

(22) Yan, D.-X.; Pang, H.; Li, B.; Vajtai, R.; Xu, L.; Ren, P.-G.; Wang, J.-H.; Li, Z.-M. Structured Reduced Graphene Oxide/Polymer Composites for Ultra-Efficient Electromagnetic Interference Shielding. *Adv. Funct. Mater.* **2015,** *25*, 559-566.

(23) Chen, Y.; Zhang, H.-B.; Yang, Y.; Wang, M.; Cao, A.; Yu, Z.-Z. High-Performance Epoxy Nanocomposites Reinforced with Three-Dimensional Carbon Nanotube Sponge for Electromagnetic Interference Shielding. *Adv. Funct. Mater.* **2016,** *26*, 447-455.

(24) Singh, S.; Tripathi, P.; Bhatnagar, A.; Prakash Patel, C. R.; Singh, A. P.; Dhawan, S. K.; Gupta, B. K.; Srivastava, O. N. A Highly Porous, Light Weight 3D Sponge Like Graphene Aerogel for Electromagnetic Interference Shielding Applications. *RSC Adv.* 2015, 5, 107083- 107087.

(25) Li, Y.; Shen, B.; Pei, X.; Zhang, Y.; Yi, D.; Zhai, W.; Zhang, L.; Wei, X.; Zheng, W. Ultrathin Carbon Foams for Effective Electromagnetic Interference Shielding. Carbon 2016, 100, 375-385.

(26) Song, W.L.; Guan, X. T.; Fan, L. Z. ; Cao, W. Q.; Wang, C. Y.; Cao, M. S. Tuning three-dimensional textures with graphene aerogels for ultra-light flexible graphene/texture composites of effective electromagnetic shielding. Carbon 2015, 93, 151-160.

(27) Shen, B.; Zhai, W.; Zheng, W. Ultrathin Flexible Graphene Film: An Excellent Thermal Conducting Material with Efficient EMI Shielding. *Adv. Functi. Mater.* **2014**, *24*, 4542-4548.

(28) Kang, J.; Kim, D.; Kim, Y.; Choi, J.-B.; Hong, B. H.; Kim, S. W. High-performance Near-field Electromagnetic Wave Attenuation In Ultra-thin and Transparent Graphene Films. *2D Mater.* **2017**, *4*, 025003.

(29) Wen, B.; Cao, M.; Lu, M.; Cao, W.; Shi, H.; Liu, J.; Wang, X.; Jin, H.; Fang, X.; Wang, W.; Yuan, J. Reduced Graphene Oxides: Light-weight and High-efficiency Electromagnetic Interference Shielding at Elevated Temperatures. *Adv. Mater.* **2014,** *26*, 3484-3849.

(30) Wen, B.; Wang, X.X.; Cao, W.Q.; Shi, H.L.; Lu, M.M.; Wang, G.; Jin, H. B.; Wang, W. Z.; Yuan, J.; Cao, M. S. Reduced Graphene Xxides: The Thinnest and Most Lightweight Materials with Highly Efficient Microwave Attenuation Performances of The Carbon World. *Nanoscale*. **2014**, *6*, 5754-5761.

(31) Thomassin, J.-M.; Jérôme, C.; Pardoen, T.; Bailly, C.; Huynen, I.; Detrembleur, C. Polymer/Carbon based Composites as Electromagnetic Interference (EMI) Shielding Materials. *Mater. Sci. Engineer. R Rep.* **2013,** *74*, 211-232.

(32) Yousefi, N.; Sun, X.; Lin, X.; Shen, X.; Jia, J.; Zhang, B.; Tang, B.; Chan, M.; Kim, J. K. Highly Aligned Graphene/Polymer Nanocomposites with Excellent Dielectric Properties for High-performance Electromagnetic Interference Shielding. *Adv. Mater.* **2014,** *26*, 5480-5487.

(33) Shen, B.; Li, Y.; Yi, D.; Zhai, W.; Wei, X.; Zheng, W. Microcellular Graphene Foam for Improved Broadband Electromagnetic Interference Shielding. *Carbon* **2016**, *102*, 154-160.

(34) Shahzad, F.; Alhabeb, M.; Hatter, C. B.; Anasori, B.; Man Hong, S.; Koo, C. M.; Gogotsi, Y. Electromagnetic Interference Shielding with 2D Transition Metal Carbides (MXenes). *Science* **2016,** *353*, 1137-1140.

(35) Shui, X.; Chung, D. D. L. Nickel Filament Polymer-matrix Composites with Low Surface Impedance and High Electromagnetic Interference Shielding Effectiveness. *J. Electr. Mater.* **1997,** *26*, 928-934.

(36) Chung, D. D. L. Electromagnetic Interference Shielding Effectiveness of Carbon Materials. *Carbon* **2001,** *39*, 279-285.

(37) Al-Saleh, M. H.; Sundararaj, U. Electromagnetic Interference Shielding Mechanisms of CNT/Polymer Composites. *Carbon* **2009,** *47*, 1738-1746.

(38) Zeng, Z.; Chen, M.; Jin, H.; Li, W.; Xue, X.; Zhou, L.; Pei, Y.; Zhang, H.; Zhang, Z. Thin and Flexible Multi-walled Carbon Nanotube/Waterborne Polyurethane Composites with High-performance Electromagnetic Interference Shielding. *Carbon* **2016,** *96*, 768-777.

(39) Zhang, L.; Liu, M.; Roy, S.; Chu, E. K.; See, K. Y.; Hu, X. Phthalonitrile-based Carbon Foam with High Specific Mechanical Strength and Superior Electromagnetic Interference Shielding Performance. *ACS Appl. Mater. Interfaces* **2016**, *8*, 7422-7430.

(40) Chen, H.; Huang, Z.; Huang, Y.; Zhang, Y.; Ge, Z.; Qin, B.; Liu, Z.; Shi, Q.; Xiao, P.; Yang, Y.; Zhang, T.; Chen, Y. Synergistically Assembled MWCNT/Graphene Foam With Highly Efficient Microwave Absorption in Both C and X bands. *Carbon* **2017**,*124*, 506-514.

(41) Wan, Y.-J.; Zhu, P.-L.; Yu, S.-H.; Sun, R.; Wong, C.-P.; Liao, W.-H., Ultralight, Super-elastic and Volume-preserving Cellulose Fiber/Graphene Aerogel for High-Performance Electromagnetic Interference Shielding. *Carbon* **2017**, *115*, 629-639.

(42) Moglie, F.; Micheli, D.; Laurenzi, S.; Marchetti, M.; Mariani Primiani, V. Electromagnetic Shielding Performance of Carbon Foams. *Carbon* **2012**, *50*, 1972-1980.

(43) Crespo, M.; González, M.; Elías, A. L.; Pulickal Rajukumar, L.; Baselga, J.; Terrones, M.; Pozuelo, J. Ultra-light Carbon Nanotube Sponge as An Efficient Electromagnetic Shielding Material in the GHz Range. *Phys. Stat. Sol. RRL* **2014,** *8*, 698-704.

(44) Hong, X.; Chung, D. D. L. Carbon nanofiber mats for electromagnetic interference shielding. *Carbon* **2017**, *111*, 529-537.

(45) Liu, W.; Zhou, R.; Zhou, D.; Ding, G.; Soah, J. M.; Yue, C. Y.; Lu, X. Lignin-assisted Direct Exfoliation of Graphite to Graphene in Aqueous Media and Its Application in Polymer Composites. *Carbon* **2015**, *83*, 188-197.

(46) Zhu, M.; Song, J.; Li, T.; Gong, A.; Wang, Y.; Dai, J.; Yao, Y.; Luo, W.; Henderson, D.; Hu, L. Highly Anisotropic, Highly Transparent Wood Composites. *Adv. Mater* **2016**, *28*, 5181-5187.

(47) Li, Y.; Shen, B.; Pei, X.; Zhang, Y.; Yi, D.; Zhai, W.; Zhang, L.; Wei, X.; Zheng, W. Ultrathin Carbon Foams for Effective Electromagnetic Interference Shielding. *Carbon* **2016**, *100*, 375-385.

(48) Wang, S-X.; Yang, L.; Stubbs, L. P.; Li, X.; He, C. Lignin-Derived Fused Electrospun Carbon Fibrous Mats as High Performance Anode Materials for Lithium Ion Batteries. *ACS Appl. Mater. Interfaces*, **2013**, *5*, 12275–12282.

(49) Zhang, H.; Cooper, A. I. Aligned Porous Structures by Directional Freezing. *Adv. Mater.* **2007,** *19*, 1529-1533.

(50) Zhang, H.; Hussain, I.; Brust, M.; Butler, M. F.; Rannard, S. P.; Cooper, A. I. Aligned Two- and Three-dimensional Structures By Directional Freezing of Polymers and Nanoparticles. *Nat. Mater.* **2005,** *4*, 787-793.

(51) Deville, S.; Saiz, E.; Nalla, R. K.; Tomsia, A. P. Freezing as a Path to Build Complex Composites. *Science* **2006**, *311*, 515-518.

(52) Jia, L.-C.; Yan, D.-X.; Yang, Y.; Zhou, D.; Cui, C.-H.; Bianco, E.; Lou, J.; Vajtai, R.; Li, B.; Ajayan, P. M.; Li, Z.-M. High Strain Tolerant EMI Shielding Using

Carbon Nanotube Network Stabilized Rubber Composite. *Adv. Mater. Technol.* **2017**, 1700078.

(53) Wu, Y.; Wang, Z.; Liu, X.; Shen, X.; Zheng, Q.; Xue, Q.; Kim, J. K. Ultralight Graphene Foam/Conductive Polymer Composites for Exceptional Electromagnetic Interference Shielding. *ACS Appl. Mater. Interfaces* **2017**, *9*, 9059-9069.

(54) Zeng, Z.; Seyed Shahabadi, S.I.; Che, B.; Zhang, Y.; Zhao, C.; Lu, X. Highly Stretchable, Sensitive Strain Sensors with Wide Linear Sensing Region Based on Compressed Anisotropic Graphene Foam/Polymer Nanocomposites. *Nanoscale* **2017**,*9*, 17396-17404.

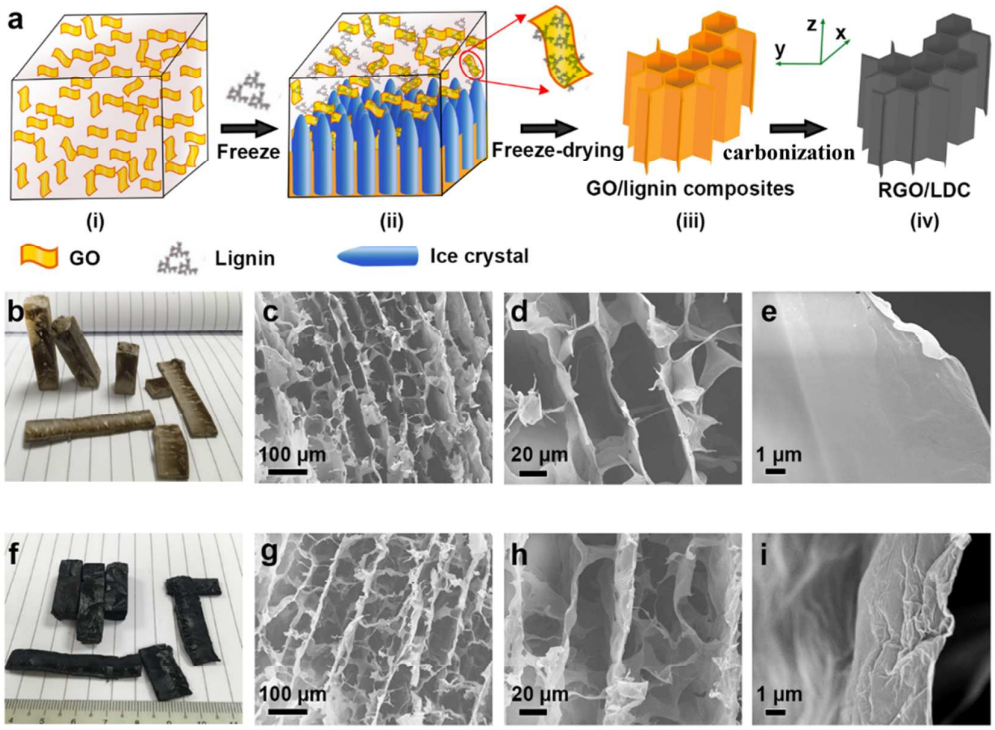

Figure 1. (a) Schematics showing the fabrication process of RGO/LDC aerogels: (i) GO aqueous dispersion, (ii) freezing process of the GO/lignin mixed aqueous suspension, (iii) GO/lignin composite foam, (iv) RGO/LDC aerogel (Z is defined as longitudinal direction, while X and Y are defined as transverse directions). Optical images showing various shapes of (b) GO/lignin porous composite foams with 25 wt% lignin (~12 mg/cm^3) and (f) the corresponding RGO/LDC porous architectures (~3.7 mg/cm^3) after carbonization; SEM images taken from the transverse direction showing microstructures of (c, d, e) the GO/lignin composite foams and (g, h, i) the corresponding RGO/LDC composite porous architectures.

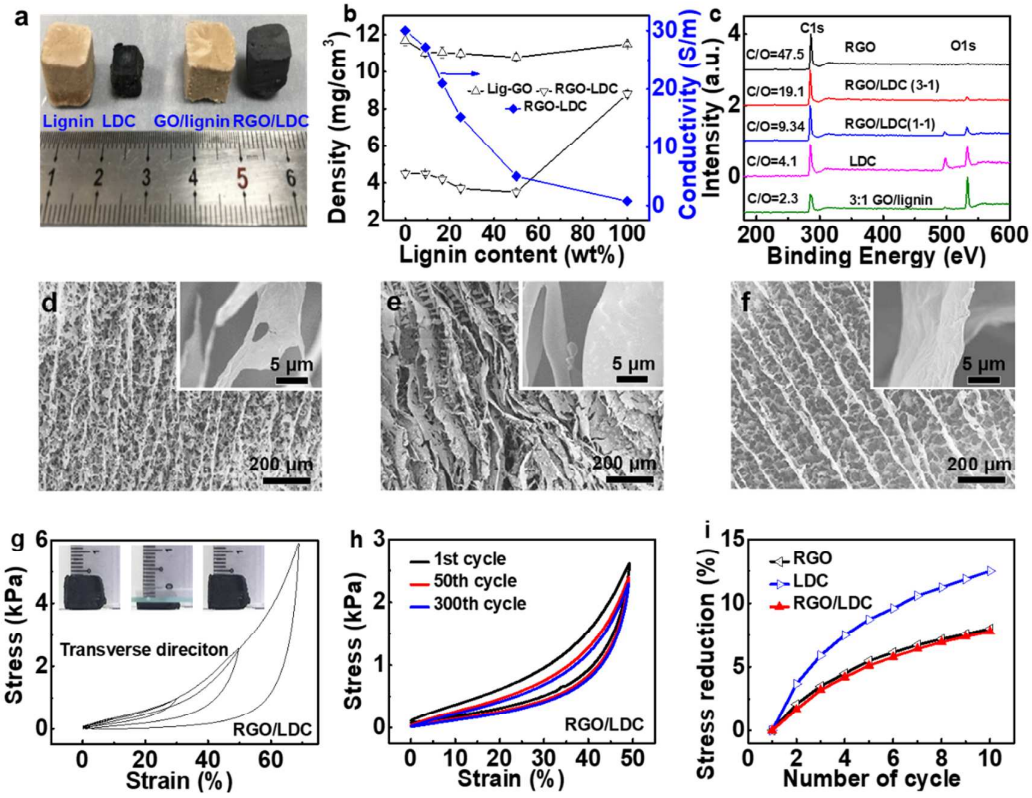

Figure 2. (a) Optical images of the porous architectures before and after carbonization; (b) densities of the GO/lignin foams and the corresponding RGO/LDC aerogels as a function of initial lignin content, as well as the electrical conductivity of the RGO/LDC aerogels; (c) XPS spectra of the GO/lignin foam with 25 wt% lignin and the carbon foams with different contents of LDC (RGO/LDC (3-1) and RGO/LDC (1-1) are made from the GO/lignin foams with 25 and 50 wt% lignin, respectively); SEM images of (d) RGO, (e) LDC and (f) RGO/LDC aerogels, of which the RGO/LDC aerogels are made from the GO/lignin foams with 25 wt% lignin; Mechanical performance of the RGO/LDC aerogels made from GO/lignin foams with 25 wt% lignin: (g) compressive behavior of the composites in transverse direction (the insert displays the compression and recovery processes), (h) transversal stress-strain curves of the architectures subjected to cyclic compression, (i) change of the maximum stress of three kinds of aligned porous aerogels in transverse direction in the first 10 compression cycles with a strain of 50 %.

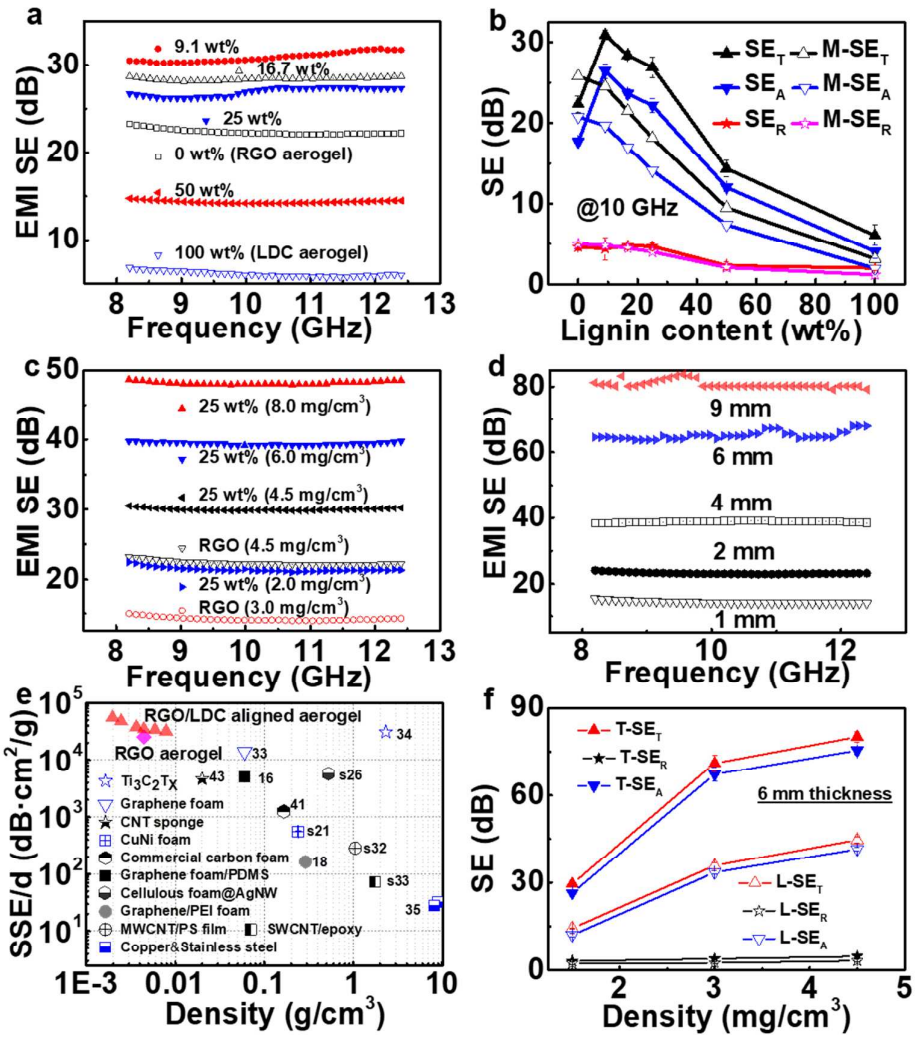

Figure 3. (a) X-band EMI SE of the aligned porous carbon architectures made from GO/lignin foams with different contents of lignin; (b) measured SE (SE_T, SE_A and SE_R) and theoretically calculated SE (M-SE_T, M-SE_A and M-SE_R) values at 10 GHz for the aligned porous carbon architectures of 2-mm thickness made from GO/lignin foams with different lignin contents; (c) X-band EMI SE of RGO and RGO/LDC composite aerogels of 2-mm thickness; (d) X-band EMI SE of the RGO/LDC aerogels at the density of 2.5 mg/cm^3 and various thickness; (e) SSE/*d* as a function of density of typical shielding materials (with cited reference); (f) longitudinal and transverse EMI SE at 10 GHz for the RGO/LDC aerogels of 6-mm thickness as a function of density. For (c)-(f), the RGO/LDC aerogels are made from GO/lignin foams with 25 wt% lignin.

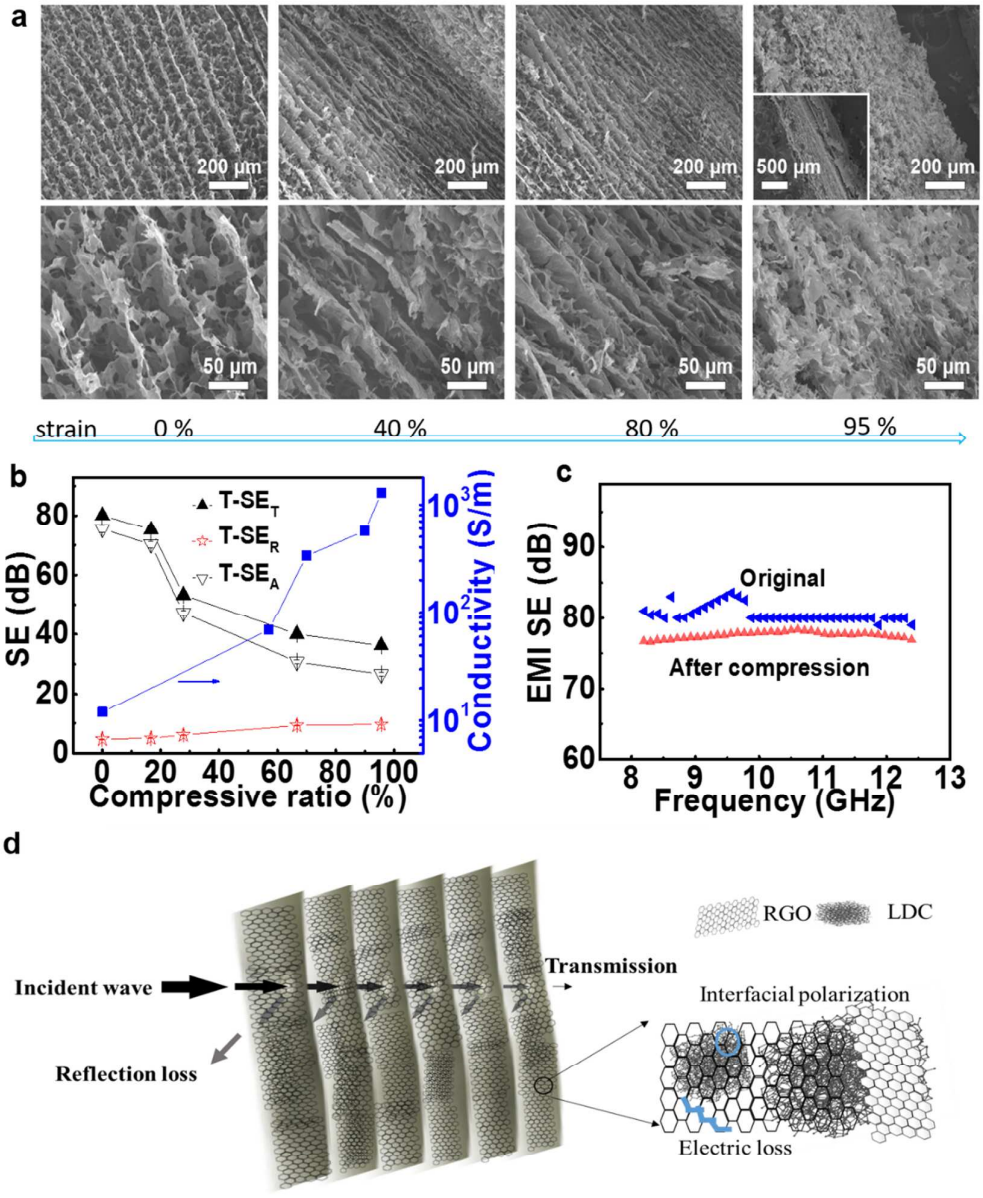

Figure 4. Microstructure and properties of the RGO/LDC aerogels under various compression ratios along transverse direction: (a) SEM images showing microstructures of the composite aerogels (the compression ratio increases from left to right), (b) EMI SE and electrical conductivity of the aerogels under various compression ratios; (c) EMI SE of the RGO/LDC aerogels before and after compression with 50 % strain for 100 cycles; (d) proposed EMI shielding mechanism for the RGO/LDC aerogels with the incident wave in the transverse direction.

Ultralight and Highly Elastic Graphene/Lignin-Derived Carbon Nanocomposite Aerogels with Ultrahigh Electromagnetic Interference Shielding Performance

Zhihui Zeng,[a] Changxian Wang,[b,c] Youfang Zhang,[a] Peiyu Wang,[c] Seyed Ismail Seyed Shahabadi,[a] Yongmao Pei,[c] Mingji Chen,[*b] and Xuehong Lu[*a]

Table of Contents / Graphic Abstract